

STEPS TOWARD DETERMINATION OF THE SIZE AND STRUCTURE OF THE BROAD-LINE REGION IN ACTIVE GALACTIC NUCLEI. XII. GROUND-BASED MONITORING OF 3C 390.3

M. DIETRICH,¹ B. M. PETERSON,² P. ALBRECHT,³ M. ALTMANN,⁴ A. J. BARTH,⁵ P. J. BENNIE,⁶ R. BERTRAM,^{2,7}
 N. G. BOCHKAREV,⁸ H. BOCK,¹ J. M. BRAUN,⁴ A. BURENKOV,⁹ S. COLLIER,⁶ L.-Z. FANG,¹⁰ O. P. FRANCIS,¹¹
 A. V. FILIPPENKO,⁵ C. B. FOLTZ,¹² W. GÄSSLER,^{1,13} C. M. GASKELL,¹¹ M. GEFFERT,⁴ K. K. GHOSH,¹⁴
 R. W. HILDITCH,⁶ R. K. HONEYCUTT,¹⁵ K. HORNE,⁶ J. P. HUCHRA,¹⁶ S. KASPI,¹⁷ M. KÜMMEL,¹
 K. M. LEIGHLY,¹⁸ D. C. LEONARD,⁵ YU. F. MALKOV,¹⁹ V. MIKHAILOV,⁹ H. R. MILLER,²⁰
 A. C. MORRILL,²¹ J. NOBLE,²² P. T. O'BRIEN,²³ T. D. OSWALT,²⁴ S. P. PEBLEY,¹¹
 M. PFEIFFER,¹ V. I. PRONIK,¹⁹ B.-C. QIAN,²⁵ J. W. ROBERTSON,¹⁵ A. ROBINSON,²⁶
 K. S. RUMSTAY,²⁷ J. SCHMOLL,^{4,28} S. G. SERGEEV,¹⁹ E. A. SERGEEVA,¹⁹
 A. I. SHAPOVALOVA,⁹ D. R. SKILLMAN,²⁹ S. A. SNEDDEN,¹¹
 S. SOUNDARARAJAPERUMAL,¹⁴ G. M. STIRPE,³⁰ J. TAO,²⁴
 G. W. TURNER,¹⁵ R. M. WAGNER,^{2,7} S. J. WAGNER,¹
 J. Y. WEI,³¹ H. WU,³¹ W. ZHENG,³² AND Z. L. ZOU³¹

Received 1997 June 13; accepted 1997 September 9

ABSTRACT

Results of a ground-based optical monitoring campaign on 3C 390.3 in 1994–1995 are presented. The broadband fluxes (B , V , R , and I), the spectrophotometric optical continuum flux $F_{\lambda}(5177 \text{ \AA})$, and the integrated emission-line fluxes of $H\alpha$, $H\beta$, $H\gamma$, $\text{He I } \lambda 5876$, and $\text{He II } \lambda 4686$ all show a nearly monotonic increase with episodes of milder short-term variations superposed. The amplitude of the continuum variations increases with decreasing wavelength (4400–9000 Å). The optical continuum variations follow the variations in the ultraviolet and X-ray with time delays, measured from the centroids of the cross-correlation functions, typically around 5 days, but with uncertainties also typically around 5 days; zero time delay between the high-energy and low-energy continuum variations cannot be ruled out. The strong optical emission lines $H\alpha$, $H\beta$, $H\gamma$, and $\text{He I } \lambda 5876$ respond to the high-energy continuum variations with time delays typically about 20 days, with uncertainties of about 8 days. There is some evidence that $\text{He II } \lambda 4686$ responds somewhat more rapidly, with a time delay of around 10 days, but again, the uncertainties are quite large (~ 8 days). The mean and rms spectra of the $H\alpha$ and $H\beta$ line profiles provide indications for the existence of at least three distinct components located at ± 4000 and 0 km s^{-1} relative to the line peak. The emission-line profile variations are largest near line center.

Subject headings: galaxies: active — galaxies: individual (3C 390.3) — galaxies: Seyfert

¹ Landessternwarte Heidelberg, Königstuhl, D-69117 Heidelberg, Germany.

² Department of Astronomy, Ohio State University, 174 West 18th Avenue, Columbus OH 43210-1106.

³ Universitätssternwarte Göttingen, Geismarlandstraße 11, D-37083 Göttingen, Germany.

⁴ Sternwarte der Universität Bonn, Auf dem Hügel 71, D-53121 Bonn, Germany.

⁵ Department of Astronomy, University of California, 601 Campbell Hall, Berkeley, CA 94720-3411.

⁶ University of St. Andrews, School of Physics and Astronomy, North Haugh, St. Andrews, Fife KY16 9SS, Scotland, UK.

⁷ Postal address: Lowell Observatory, 1400 Mars Hill Road, Flagstaff, AZ 86001.

⁸ Sternberg Astronomical Institute, Universitetskij Prospekt, 13, 119899 Moscow, Russia.

⁹ Special Astrophysical Observatory, Russian Academy of Science, Nyzknij Arkhyz, Karachaj-Cherkess Republic, 357147, Russia.

¹⁰ Department of Physics, University of Arizona, Tucson, AZ 85721.

¹¹ University of Nebraska, Lincoln, Department of Physics and Astronomy, Lincoln, NE 68588-0111.

¹² MMT Observatory, University of Arizona, Tucson, AZ 85721.

¹³ Universitätssternwarte München, Scheinerstrasse 1, D-81679 München, Germany.

¹⁴ Indian Institute of Astrophysics, Vainu Bappu Observatory, Kavalur, Alangayam, N.A.A. 635 701, T.N., India.

¹⁵ Department of Astronomy, Indiana University, 319 Swain West, Bloomington, IN 47405.

¹⁶ Harvard-Smithsonian Center for Astrophysics, 60 Garden Street, Cambridge, MA 02138.

¹⁷ Department of Physics and Astronomy, Tel Aviv University, Tel Aviv 69978, Israel.

¹⁸ Columbia Astrophysics Laboratory, Columbia University, 538 West 120th Street, New York, NY 10027.

¹⁹ Crimean Astrophysical Observatory, p/o Nauchny, 334413 Crimea, Ukraine.

²⁰ Department of Physics and Astronomy, Georgia State University, Atlanta, GA 30303.

²¹ Center for Space Physics, Boston University, 725 Commonwealth Avenue, Boston, MA 02215.

²² Center for Automated Space Sciences, Department of Physics and Astronomy, Western Kentucky University, Bowling Green, KY 42101-3576.

²³ Department of Physics & Astronomy, University of Leicester, University Road, Leicester LE1 7RH, UK.

²⁴ Department of Physics and Space Science, Florida Institute of Technology, 150 West University Avenue, Melbourne, FL 32901-6988.

²⁵ Shanghai Observatory, The Chinese Academy of Sciences, 80 Nandan Road, Shanghai 200030, China.

²⁶ Division of Physics and Astronomy, Department of Physical Science, University of Hertfordshire, College Lane, Hatfield, Herts AL10 9AB, UK.

²⁷ Department of Physics, Astronomy, and Geology, Valdosta State University, Valdosta, GA 31698-0055.

²⁸ Astrophysikalisches Institut Potsdam, An der Sternwarte 16, D-14482 Potsdam, Germany.

²⁹ Center for Basement Astrophysics, 9517 Washington Avenue, Laurel, MD 20723.

³⁰ Osservatorio Astronomica di Bologna, Via Zamboni 33, I-40126 Bologna, Italy.

³¹ Beijing Astronomical Observatory, Beijing 100080, Beijing, China.

³² Center for Astrophysical Sciences, John Hopkins University, Baltimore, MD 21218.

1. INTRODUCTION

Intensive multiwavelength monitoring campaigns have shown that variability studies provide an excellent tool to investigate the innermost region of active galactic nuclei (AGNs). Detailed studies of the continuum and emission-line variations have revealed new insights about the size, structure, and dynamics of the broad-line region (BLR) in these sources (see Peterson 1993 for a review).

Over the last decade, a number of large space-based and ground-based AGN monitoring programs have been undertaken. Our own group, the International AGN Watch consortium (Alloin et al. 1994), has undertaken monitoring programs on several Seyfert galaxies, including programs on NGC 5548 (Clavel et al. 1991; Peterson et al. 1991, 1993, 1994; Maoz et al. 1993; Dietrich et al. 1993; Korista et al. 1995), NGC 3783 (Reichert et al. 1994; Stirpe et al. 1994; Alloin et al. 1995), NGC 4151 (Crenshaw et al. 1996; Kaspi et al. 1996; Warwick et al. 1996; Edelson et al. 1996), Fairall 9 (Rodríguez-Pascual et al. 1997; Santos-Lleó et al. 1997), and NGC 7469 (Wanders et al. 1997; Collier et al. 1998). In late 1994, the International AGN Watch began a multi-wavelength monitoring campaign on the broad-line radio galaxy (BLRG) 3C 390.3, a prominent nearby ($z = 0.0561$; Osterbrock, Koski, & Phillips 1975) AGN with broad double-peaked emission-line profiles (Sandage 1966; Lynds 1968). 3C 390.3 has a well-known variability history (see, e.g., Selmes, Tritton, & Wordsworth 1975; Barr et al. 1980; Penston & Pérez 1984; Veilleux & Zheng 1991; Zheng 1996; Wamsteker et al. 1997). Zheng (1996) and Wamsteker et al. (1997) analyzed the *IUE* spectra of 3C 390.3 that have been taken from 1978 until 1992. The variable broad Ly α and C IV emission are delayed by ~ 60 days with respect to the UV continuum variations.

3C 390.3 is an extended double-lobed FR II radio source (Leahy & Perley 1995) with a $60''$ one-sided narrow jet at $PA = -37^\circ$, and it is one of the rare lobe-dominated radio galaxies which show superluminal motions, with $v/c \approx 4.0$ (Alef et al. 1996). This is the first time that variations in a radio-loud AGN have been studied over a broad energy range (from radio to X-ray energies) for an extended period (1 yr)—the observations obtained for this program cover over eight decades in frequency. The results of the X-ray and ultraviolet monitoring campaigns performed with *ROSAT* and the *IUE* satellite will be presented in Leighly et al. (1997) and O'Brien et al. (1998), respectively.

In this contribution, we present the optical photometric and spectroscopic observations that were obtained as part of this monitoring program; observations in other wavelength bands will be presented elsewhere. In § 2, we describe the optical observations and outline intercalibration procedures by which a homogeneous set of the photometric and spectroscopic measurements is achieved. In § 3, we highlight emission-line profile variations based on mean and rms spectra and present the results of some preliminary time-series analysis. We summarize our results in § 4.

2. OBSERVATIONS AND DATA ANALYSIS

Spectra and broadband photometric measurements of 3C 390.3 were obtained by a large number of observers between 1994 October and 1995 October. Table 1 gives a brief overview of the various sources of the data we report here. Each group (col. [1]) was assigned an identification code given in column (2) which will be used throughout this

paper. Column (3) gives the aperture of the telescope used. Columns (4)–(7) list the focal-plane apertures used in various observations; generally, fixed instrument apertures were used, although two groups (F, N) adjusted their aperture to compensate for changes in seeing. In most cases the size of the apertures corresponds to 3 times the average seeing at the observing site. Those large apertures cover the AGN as well as the entire galaxy. In column (8), the spectrograph slit widths (in the dispersion direction) and extraction widths (cross-dispersion dimension), respectively, of the spectra are listed.

Complete logs of the photometric and spectroscopic observations (Tables 2 and 3) are available as electronic files on the WWW at the URL given in the following: <http://www.astronomy.ohio-state.edu/~agnwatch/>.

2.1. Optical Photometry

The photometric observations were made through different combinations of broadband filters. Generally, the brightness of 3C 390.3 was scaled with respect to standard stars in the photometric sequence (stars A, B, and D) defined by Penston, Penston, & Sandage (1971), plus a *Hubble Space Telescope* (HST) guide star located at $208''$ from 3C 390.3 at $PA = 106^\circ$ (HST GS 4591:731). In some cases, star A could not be used because of saturation.

The colors of the comparison stars (B, D, and HST GS 4591:731) differ by up to 0.1 mag, while star A is ~ 2.5 mag. brighter than the mean values of these three stars. The mean colors of 3C 390.3 are similar to the mean colors of the comparison stars within 0.2 mag. Since the stars and the AGN are within the same field of view of the CCD images, effects of different spectral energy distributions and air masses on the internal calibration can be neglected.

In the following, the procedure we use to derive the *R*-band magnitudes will be described in some detail. The light curves of the other broadband measurements were obtained in a similar way.

2.1.1. *R* Band

First, a subsample was selected that covered the entire monitoring campaign with a good temporal sampling rate. For the *R*-band measurements, the observations recorded with the 0.7 m telescope of the Landessternwarte Heidelberg (L) provide an appropriate data set. The aperture used was a $15''$ rectangle to ensure that the light loss can be neglected even in the case of bad seeing. The frames were bias and flat-field corrected in the standard way. In the next step, the brightness of 3C 390.3 was measured with respect to the comparison stars in the same field, yielding the difference in apparent magnitude between 3C 390.3 and the comparison stars. In the *R* band, stars B and D from Penston et al. (1971) and HST GS 4591:731 mentioned above were used for calibration. The *R*-band magnitudes that were derived for these stars are presented in Table 4 together with the *B* and *V* magnitudes from Penston et al. (1971). Finally, the *R*-band light curves of the other subsamples were shifted to the *R*-band light curve derived from the Heidelberg sample by applying a constant additive magnitude offset to all of the measurements in a given subset. The additive factor was derived by comparison of *R*-band magnitudes that were observed within ± 3 days. The additive factors for the individual subsamples are presented in Table 5. The additive scaling factors given in Table 5 are quite large in some cases. Generally, the brightness variations of

TABLE 1
OVERVIEW OF OBSERVATIONS

SOURCE (1)	CODE (2)	TELESCOPE (m) (3)	PHOTOMETRY APERTURE (arcsec)				SPECTROSCOPY APERTURE (arcsec) (8)
			B (4)	V (5)	R (6)	I (7)	
Perkins reflector, Lowell Observatory ^a	A	1.8	5 × 7.5
Shane reflector, Lick Observatory ^a	B	3.0	4 × 10, 2 × 5.6
Mt. Hopkins Observatory	C	1.6	3 × 3, 2 × 3, 1 × 3
Shajn reflector, Crimean Observatory	D	2.6	3 × 11
Beijing Observatory	E	2.2	4 × 7.2, 4 × 8.4, 4 × 12, 4 × 10.3, 4 × 3.6, 2.5 × 9.6, 3.5 × 9.6
Steward Observatory	F	2.3	2.5–3.3 ^b	2.5–3.3 ^b	2.5–3.3 ^b	...	2.5 × 12
Calar Alto Observatory	G1	1.2	25.0	25.0	...
Calar Alto Observatory	G2	2.2	14.0	14.0	14.0	14.0	2 × 14.1, 2 × 10
MMT Observatory	H	4.5	2 × 10, 1 × 7.2, 2 × 6
Isaac Newton Telescope	I	2.5	1.62 × 6.5
Special Astrophysical Observatory	J	1.0	4.0, 4.4	5.3, 4.8	5.4, 8.0
Special Astrophysical Observatory	J	6.0	3 × 3.6, 3.6 × 3.6
McDonald Observatory	K	2.7	2 × 7.2
Landessternwarte Heidelberg ^c	L	0.7	15.0	15.0	...
James Gregory Telescope, St. Andrews	M	0.9	...	47.0	47.0	47.0	...
RoboScope, Indiana University	N	0.4	...	var. ^b
Wise Observatory ^d	O	1.0	10.0	10.0	12.0	12.0	...
Vainu Bappu Observatory	P1	2.3	...	7.85
Vainu Bappu Observatory	P2	1.0	...	6.06
Behlen Observatory ^e	Q	0.8	...	13.7
Center for Basement Astrophysics	R	0.7	...	6.0	6.0	6.0	...
Hoher List Observatory, Bonn	S1	0.6	...	3.0	3.0
Hoher List Observatory, Bonn	S2	0.4	...	5.0	5.0
SARA Telescope, Kitt Peak	T	0.9	20.0	...
Shanghai Observatory	U	1.6	...	6–7.5	6–7.5	6–7.5	...

^a Obtained spectra were used to build up the light curves.
^b Aperture was optimized with respect to the seeing during the exposure.
^c Obtained broadband measurements (*R*, *I*) were used to build up the light curves.
^d Obtained broadband measurements (*B*) were used to build up the light curves.
^e Obtained broadband measurements (*V*) were used to build up the light curves.

TABLE 2
PHOTOMETRIC OBSERVATIONS

UT Date	JD (2,400,000+)	Code	Seeing (arcsec)	B (10^{-15} ergs s $^{-1}$ cm $^{-2}$ Å $^{-1}$)	V (10^{-15} ergs s $^{-1}$ cm $^{-2}$ Å $^{-1}$)	R (10^{-15} ergs s $^{-1}$ cm $^{-2}$ Å $^{-1}$)	I (10^{-15} ergs s $^{-1}$ cm $^{-2}$ Å $^{-1}$)
1994 Oct 18	49644.40	L	8.1	1.834 ± 0.017	...
1994 Oct 20	49646.29	L	6.7	1.826 ± 0.017	...
1994 Nov 3	49660.36	L	4.8	1.827 ± 0.017	...
1994 Nov 3	49660.40	L	6.8	1.167 ± 0.018
1994 Nov 13	49670.31	M	1.865 ± 0.103

NOTE.—Table 2 appears in its entirety in the electronic edition of the *Astrophysical Journal Supplement Series*.

3C 390.3 were provided in magnitudes using the standard stars in the field for calibration. But a few groups (M, R, U) provided the brightness of 3C 390.3 as differential magnitudes relative to the calibration stars in the field.

2.1.2. B Band

The B -band magnitudes are scaled with respect to the measurements taken at Wise Observatory (O). The offset for the Steward Observatory sample (F) was derived by comparison of epochs that were simultaneous to within ± 3 days. This restriction could not be used for the Special Astrophysical Observatory (J); in this case, the offset is based on epochs separated by no more than 6 days. The resulting additive scaling factors are given in Table 5.

2.1.3. V Band

The sample recorded at Behlen Observatory (Q) was used as the standard in the V band because the temporal sampling is good and the measurements were made through a large aperture (13"7) so that uncertainties due to seeing variations are small. The V -band measurements are made relative to star B, which is close in brightness to the nucleus of 3C 390.3. In order to scale the V magnitudes to a common flux level, we compared measurements at epochs separated by no more than 3 days. In Table 5, the differential magnitudes are given that were applied to the individual light curves to produce a common light curve.

2.1.4. I Band

For the calibration of the I -band magnitudes, we used observations taken at Calar Alto Observatory. The I -band frames were recorded in 1994 December. The calibration was based on the globular cluster NGC 2419 using the stars given by Christian et al. (1985). The resulting brightnesses of stars A, B, D, and HST GS 4591:731 are given in Table 4. The additive factors for the individual subsamples are presented in Table 5.

The measured brightnesses of the stars used for calibration are in good agreement with the values provided by Penston et al. (1971). However, star A deviates from this

trend in R and I in comparison to stars B and D. It might be that this is due to the brightness of star A causing nonlinearity effects and an underestimate of the brightness of star A. After combining the measurements of the individual groups to common broadband light curves, the apparent magnitudes were transformed into flux. The conversion has been performed using the following equations (Allen 1973; Wamsteker 1981):

$$\begin{aligned}\log F_{\lambda}(4400 \text{ \AA}) &= -0.4m_B - 8.180, \\ \log F_{\lambda}(5500 \text{ \AA}) &= -0.4m_V - 8.439, \\ \log F_{\lambda}(7000 \text{ \AA}) &= -0.4m_R - 8.759, \\ \log F_{\lambda}(9000 \text{ \AA}) &= -0.4m_I - 9.080.\end{aligned}\quad (1)$$

The resulting time-binned light curves from the B , V , R , and I broadband measurements in units of 10^{-15} ergs s $^{-1}$ cm $^{-2}$ Å $^{-1}$ are displayed in Figure 1.

2.2. Optical Spectroscopy

The flux calibration of AGN spectra can be accomplished in several ways. In variability studies, it is common practice to normalize the flux scale to the fluxes of the narrow emission lines, which are assumed to be constant over timescales of at least several decades (Peterson 1993). This assumption is justified by the large spatial extent and low gas density of the narrow-line region (NLR), since light-travel-time effects and the long recombination timescale ($\tau_{\text{rec}} \approx 100$ yr for $n_e \approx 10^3$ cm $^{-3}$) damp out short timescale variability. However, 3C 390.3 is apparently a special case in this regard, as narrow-line variability has been reported in this object (Clavel & Wamsteker 1987). On the basis of spectra obtained between 1974 and 1990, Zheng et al. (1995) present evidence that the [O III] $\lambda\lambda 4959, 5007$ fluxes follow the variations in the continuum, although on a longer timescale than the broad emission lines. During the period of decreasing and increasing [O III] flux, there might also be periods of several months or a year of nearly constant [O III] flux. However, we need to examine the data closely to test for variability of the [O III] lines before we use them for flux calibration.

Two data sets, the Ohio State sample (A) and the Lick

TABLE 3
LOG OF SPECTROSCOPIC OBSERVATIONS

UT Date	JD (2,400,000+)	Code	Seeing (arcsec)	Aperture (arcsec)	P.A. (deg)	Wavelength (Å)	Resolution (Å)	File Name
1994 Jun 14	49517.8450	F	2.0	2.5×12	90	4900–8400	8.0	c49517fe
1994 Aug 30	49595.3892	G	...	2.0×14.1	90	4517–8500	10.0	c49594ga
1994 Aug 30	49595.4112	G	...	2.0×14.1	90	4517–8500	10.0	c49594gb
1994 Sep 1	49597.4350	D	2.8	3×11	90	6314–7496	...	c49596dr
1994 Sep 4	49600.4360	D	3.0	3×11	90	6335–7541	...	c49599dr

NOTE.—Table 3 appears in its entirety in the electronic edition of the *Astrophysical Journal Supplement Series*.

TABLE 4
ADOPTED MAGNITUDES FOR STANDARD STARS

Star	B^a	V^a	R^b	I^b
A (HST GS 4591:756).....	12.74	11.71	12.11	11.34
B (HST GS 4591:850).....	15.04	14.28	14.13	13.59
D (HST GS 4591:865).....	15.40	14.65	14.42	13.90
(HST GS 4591:731).....	14.86	14.17	14.09	13.57

^a From Penston, Penston, & Sandage 1971. Estimated uncertainty 0.02 mag.

^b From Calar Alto 2.2 m telescope observations, 1994 December. Estimated uncertainty 0.01 mag (R) and 0.04 mag (I)

Observatory sample (B), were selected to measure the absolute flux in the $[\text{O III}] \lambda 5007$ line. The spectra were photometrically calibrated by comparison with the broadband photometric measurements. The spectra were convolved with the spectral response curve of the Johnson V and R filters (Schild 1983), and the flux of the convolved spectra was measured for the wavelength range of the filter curves and compared with photometric data points. Photometric and spectroscopic data obtained no more than 3 days apart were used in this comparison. The spectra were then scaled by multiplicative factors to achieve the same total flux ratio as the intercalibrated photometric measurements in V and R . For the Lick data (B), the R -band measurements were used to scale the entire spectrum, and the $[\text{O III}] \lambda 5007$ flux was then measured. Spectra from the Ohio State sample (A) do not cover the entire wavelength range of the V -band filter, and therefore the missing contribution to the V -band measurement was estimated from the Lick spectra, which cover the entire wavelength range of the V bandpass. The ratio of V -band flux measured from the Ohio State spectra to that measured from the Lick spectra was found to be 0.830 ± 0.002 , i.e., a constant contribution. The fluxes from the Ohio State spectra were thus corrected by this constant factor.

The $[\text{O III}] \lambda 5007$ flux was then measured from the photometrically scaled Ohio State (A) and Lick Observatory (B) spectra by integrating the spectrum over the range 5258–5320 Å. Therefore, a linear pseudocontinuum was

fitted beneath the $[\text{O III}] \lambda 5007$ emission line. In Figure 2, we show the $[\text{O III}] \lambda 5007$ flux measured from the Ohio State and Lick subsets normalized to a mean value of unity and displayed as a function of time. No time-dependent trend is detected, and the rms variation about the mean is $\sim 2.6\%$. We thus conclude that it is safe to assume that the $[\text{O III}] \lambda 5007$ flux is constant within a few percent over the duration of this monitoring program and that the $[\text{O III}] \lambda 5007$ flux can be used to calibrate all of the spectra. The $[\text{O III}] \lambda 5007$ flux is taken to be $F([\text{O III}] \lambda 5007) = 1.44 \times 10^{-13} \text{ ergs s}^{-1} \text{ cm}^{-2}$, the mean value of the data points plotted in Figure 2.

It is also important to take aperture effects into account (Peterson & Collins 1983). The seeing-dependent uncertainties that are introduced by the aperture geometry can be minimized by using large apertures. It has been shown that apertures of $5'' \times 7''.5$ can reduce seeing-dependent photometric errors to no more than a few percent in the case of nearby AGNs (Peterson et al. 1995). In the case of 3C 390.3, the BLR and the NLR can be taken to be point sources (see Baum et al. 1988), which means that no aperture correction needs to be made for the AGN continuum/narrow-line flux ratios or the broad-line/narrow-line ratios, since seeing-dependent light losses at the slit will be the same for each of these components. However, the amount of host-galaxy starlight that is recorded is still aperture dependent, and systematic corrections need to be employed.

In order to estimate how sensitive the measurements are to seeing-dependent light loss from the host galaxy, we carried out simulated aperture photometry on the R -band frame obtained at Calar Alto with the 2.2 m telescope under good seeing conditions ($\sim 0''.7$). The host galaxy has been separated from the pointlike AGN component by fitting a de Vaucouleurs $r^{1/4}$ profile to the observed surface-brightness distribution. This image was convolved with Gaussians of various width to simulate various seeing conditions up to $4''.0$. The flux of the host galaxy and of the pointlike AGN were measured for a fixed aperture of $10''.5 \times 10''.5$. The flux ratio of the pointlike AGN to the host galaxy for the R band is $F_{\text{AGN}}/F_{\text{galaxy}} = 0.63 \pm 0.03$. This is similar to the result of Smith & Heckman (1989), who found $F_{\text{AGN}}/F_{\text{galaxy}} = 0.44$ for V -band measurements. By using dif-

TABLE 5
SCALING FACTORS FOR PHOTOMETRIC SUBSETS

SAMPLE	ADDITIVE CONSTANT (mag)			
	B^a	V^b	R^c	I^c
N	-0.207 ± 0.065
F	$+1.029 \pm 0.024$	-0.240 ± 0.001	$+2.125 \pm 0.013$...
G1	$+0.007 \pm 0.007$	$+0.244 \pm 0.000$
G2	14.074	0.305
J	-0.440 ± 0.000	-0.267 ± 0.072	$+0.080 \pm 0.012$...
M	$+13.499 \pm 0.039$	$+13.099 \pm 0.065$	$+13.246 \pm 0.033$
O	-0.022 ± 0.001	-0.101 ± 0.019	$+0.138 \pm 0.000$
P1	-0.131 ± 0.075
P2	-0.120 ± 0.000
R	-0.380 ± 0.000	$+11.070 \pm 0.070$	$+11.189 \pm 0.000$
S1	-0.230 ± 0.000	-0.885 ± 0.047	...
S2	-0.080 ± 0.000	-0.841 ± 0.008	...
T	$+0.300 \pm 0.000$
U	$+11.480 \pm 0.051$	$+10.939 \pm 0.044$	$+11.091 \pm 0.047$

^a Relative to Wise Observatory subset (O).

^b Relative to Behlen Observatory subset (Q).

^c Relative to Landessternwarte Heidelberg subset (L). Calibration based on observations with Calar Alto 2.2 m telescope, 1994 December.

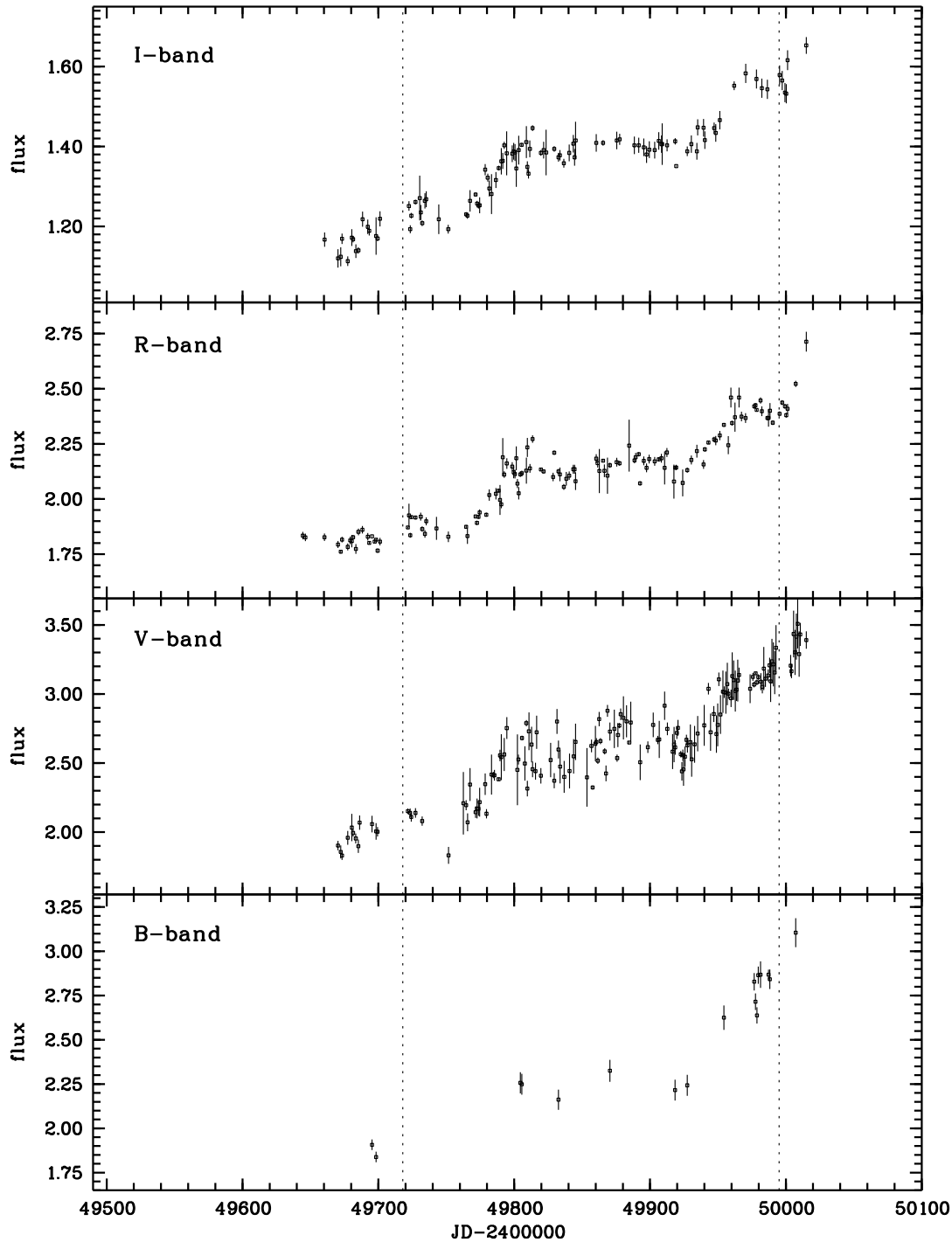


FIG. 1.—Optical broadband light curves of 3C 390.3 from 1994 October to 1995 October. Fluxes are in units of 10^{-15} ergs $\text{s}^{-1} \text{cm}^{-2} \text{\AA}^{-1}$. The larger uncertainties of the *V*-band measurements might be due to a lower signal than in the *R*-band measurements that contain the broad $\text{H}\alpha$ emission. The dashed vertical lines mark the temporal range of the X-ray observations.

ferent aperture geometries in these simulations, we find that the ratio of AGN light to starlight from the host galaxy changes over the full range of observed seeing values by less than 1% for the larger apertures (i.e., slit width greater than $4''$). For intermediate slit widths ($2''.5$ – $3''.6$), seeing variations introduce uncertainties of $\sim 5\%$. For the smallest slit widths ($\leq 2''.5$), seeing effects can alter the nucleus to starlight ratio by as much as $\sim 10\%$, with the largest uncertainties occurring for seeing worse than $\sim 3''$.

2.3. Intercalibration of the Spectra

Since the data that constitute the various samples were taken with different instruments in different configurations, the spectra have to be intercalibrated to a common flux level. As we have shown above, the $[\text{O III}] \lambda 5007$ line flux was constant to better than 3% during this campaign, so we can safely use the narrow emission lines as flux standards. In order to avoid any wavelength-dependent calibration

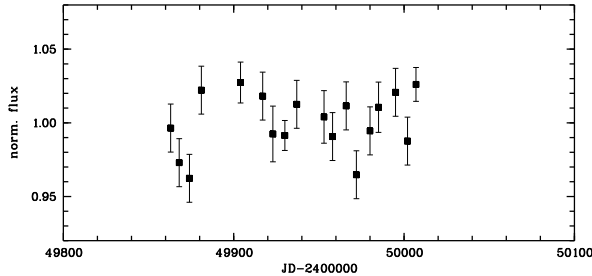


FIG. 2.—Normalized [O III] $\lambda 5007$ flux measured from photometrically calibrated spectra from Ohio State (A) and Lick Observatory (B) shown as a function of time. The data show no clear time dependence, and the scatter about the mean is about 2.6%. The narrow-line [O III] flux thus appears to be constant over the timescales of interest, and can be used to calibrate the fluxes of all the spectra.

errors, each spectrum was scaled in flux locally over a limited wavelength range prior to measurement. The $H\beta$ spectral region was scaled with respect to the [O III] $\lambda\lambda 4959, 5007$ line fluxes, while the $H\alpha$ region was scaled with respect to the fluxes of the [O I] $\lambda 6300$ and [N II] $\lambda\lambda 6548, 6584$ emission lines. The spectra were intercalibrated using the method described by van Groningen & Wanders (1992). This procedure corrects the data for different flux scales, small wavelength shifts, and different spectral resolutions by minimizing the narrow-line residuals in difference spectra formed by subtracting a “reference spectrum” from each of the observed spectra. The rescaled spectra are used to derive integrated emission-line fluxes as well as the optical continuum flux.

The continuum fluxes are then adjusted for different amounts of host-galaxy contamination (see Peterson et al.

1995 for a detailed discussion) through the relationship

$$F_{\lambda}(5177\text{\AA}) = F_{5007} \left[\frac{F_{\lambda}(5177\text{\AA})}{F([\text{O III}]\lambda 5007)} \right]_{\text{obs}} - G, \quad (2)$$

where F_{5007} is the adopted absolute [O III] $\lambda 5007$ flux, the quantity in brackets is the observed continuum-to-[O III] $\lambda 5007$ flux ratio measured from the spectrum, and G is an aperture-dependent correction for the host-galaxy flux. The Ohio State sample (A), which uses a relatively large aperture ($5'' \times 7''.5$), was adopted as a standard (i.e., $G = 0$ by definition), and other data sets were merged progressively by comparing measurements based on observations made no more than ± 3 days apart. This means that any real variability that occurs on timescales this short tends to be somewhat suppressed by the process that allows us to combine the different data sets. The additive scaling factor G for the various samples are given in Table 6.

3. RESULTS

3.1. Light Curves

The average interval between measurements is about 2 ± 0.5 days for V , R , and I , while the B -band variations have been measured with an average sampling interval of 16 ± 18 days (Table 7). The time-binned broadband continuum light curves are shown in Figure 1. The variations can be characterized as a nearly monotonic increase of the flux with smaller scale variations superposed on this general trend. From JD 2,449,760 to JD 2,449,800, the flux rose in the V , R , and I bands faster than during the previous interval. After this period, the flux level stays nearly constant for nearly 3 months, and then a second strong increasing episode follows. The V -band light curve appears to have more complicated structure, and we note in particular apparently rapid variations during the interval JD 2,449,800 to JD 2,449,920.

Figure 3 shows two spectra of 3C 390.3 that represent the low- (JD 2,449,636) and high- (JD 2,450,007) flux states observed during this campaign. The most obvious variation is the strong increase of the small blue bump, the very broad feature shortward of 4000\AA , which is usually ascribed to Balmer continuum emission and a blend of several thousand Fe II emission lines (Wills, Netzer, & Wills 1985). The broad Balmer lines show also evidence for increasing flux. Underneath the low-state spectrum in Figure 3 we show the integration ranges for the various features that have been measured in these spectra. The optical emission-line fluxes were integrated over a common range of $\pm 7500\text{ km s}^{-1}$ for the strong Balmer emission lines ($H\alpha$, $H\beta$, and $H\gamma$) and He I $\lambda 5876$. The He II $\lambda 4686$ line flux was integrated over a range corresponding -7500 km s^{-1} to $+4000\text{ km s}^{-1}$ to reduce contamination by $H\beta$ (see Table 8). A local linear continuum fit was interpolated under each emission line. In the case of the $H\beta$ region, the continuum was defined by the

TABLE 6
EXTENDED SOURCE CORRECTION
FACTOR G

Data Set	G ($10^{-15}\text{ ergs s}^{-1}\text{ cm}^{-2}\text{\AA}^{-1}$)
A	0.00
B	0.79 ± 0.40
C	1.17 ± 0.64
D	-0.22 ± 0.40
E	1.35 ± 0.93
F	1.21
G2	1.23
G2	0.79 ± 0.40
H	1.57
H	3.29 ± 0.22
I	1.58 ± 0.93
J	1.43
K	1.09 ± 0.37

TABLE 7
SAMPLING CHARACTERISTICS

Feature	N	Interval (days)	Feature	N	Interval (days)
B	21	15.6 ± 17.8	$H\gamma$	55	8.2 ± 14.0
V	244	1.4 ± 2.5	He II $\lambda 4686$	100	4.8 ± 9.1
R	206	1.8 ± 2.7	$H\beta$	104	5.3 ± 11.2
I	149	2.4 ± 3.4	He I $\lambda 5876$	60	9.3 ± 17.0
$F_{\lambda}(5177\text{\AA})$	97	5.7 ± 12.8	$H\alpha$	84	6.6 ± 15.5

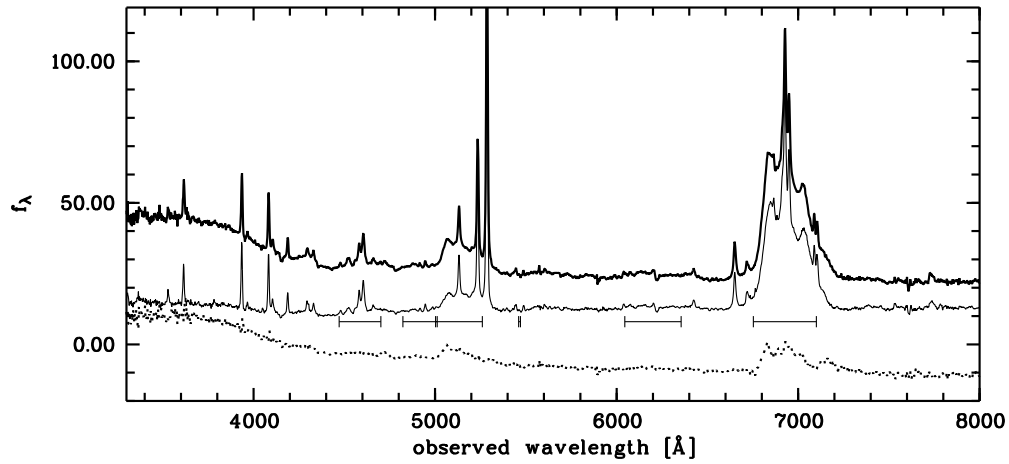


FIG. 3.—Spectra from Lick Observatory (B) that illustrate the high-flux (JD 2,450,007; *thick line*) and low-flux (JD 2,449,636; *thin line*) extremes observed during this campaign. The integration ranges are marked underneath the spectra for the measured line emission (*left to right*: $H\gamma$, $\text{He II } \lambda 4686$, $H\beta$, $F_\lambda(5177 \text{ \AA})$, $\text{He I } \lambda 5876$, and $H\alpha$). The vertical scale is in units of $10^{-16} \text{ ergs s}^{-1} \text{ cm}^{-2} \text{ \AA}^{-1}$. Note the dramatic variability of the “small blue bump,” i.e., the very broad feature that dominates the spectrum shortward of about 4200 \AA . At the bottom of the figure the difference spectrum corresponding to the low and high state is shown as a thick dotted line.

flux measured in two narrow (10 \AA width) windows at 4400 \AA and 5475 \AA in the observed frame. Although the region of the long-wavelength window might be contaminated by several weak emission lines and the Mg *b* absorption feature, this is still the most line-free region near $H\beta$ and is thus an appropriate place to estimate the optical continuum flux. The continuum window at 4400 \AA is displaced from the $H\gamma$ line center by $\sim 12,000 \text{ km s}^{-1}$, and thus possible contamination by broad emission line flux can be safely ignored (see Fig. 3). Contamination of $H\beta$ by $[\text{O III}]$ emission has been corrected by subtracting the constant $[\text{O III}] \lambda 5007$ flux given earlier plus the $[\text{O III}] \lambda 4959$ flux which we account for by assuming a $[\text{O III}] \lambda 5007/[\text{O III}] \lambda 4959$ flux ratio of 3. In the case of the $H\alpha$ region, two narrow (10 \AA in width) windows at 5960 \AA and 7495 \AA were used to define the continuum underlying the lines. No attempt has been made to correct any of the measured emission-line fluxes for

their respective narrow-line contributions. In each spectrum, the optical continuum flux measured is the average value in the range 5460–5470 \AA . The extracted range of the emission lines and of the optical continuum is given in Table 8.

The time-binned light curves for the strong emission lines and the optical continuum flux $F_\lambda(5177 \text{ \AA})$ measured from the calibrated spectra are plotted in Figure 4. The corresponding flux measurements are available on the WWW at the URL given above (Table 9).

A final check of the uncertainty estimates was performed by examining the ratios of all pairs of photometric and spectroscopic observations which were separated by 2 days or less. The error estimates were also calculated using maximum intervals of 3 days and 4 days, and the resulting errors are identical to within 3%. Generally, there are at least a few hundred independent pairs of measurements within 2 days of one another for the photometric measurements. Only the *B*-band curve yields fewer independent pairs. For the spectroscopic data, the number of independent pairs is of the order of several dozen with the exception of $H\gamma$. The dispersion about the mean (unity), divided by $2^{1/2}$, provides an estimate of the typical uncertainty in a single measurement (σ_{est}). The observational uncertainties (σ_{obs}) assigned to the spectral flux measurements were estimated from the error spectra that were calculated within the intercalibration routine, as well as from the signal-to-noise ratio within the spectral range near the individual emission

TABLE 8
INTEGRATION LIMITS

Feature	Wavelength Range (\AA)
$H\alpha \lambda 6563$	6753–7100
$\text{He I } \lambda 5876$	6045–6355
$F_\lambda(5177 \text{ \AA})$	5460–5470
$H\beta \lambda 4861$	5003–5260
$\text{He II } \lambda 4686$	4823–5012
$H\gamma \lambda 4340$	4472–4701

TABLE 9
LIGHT CURVES

JD ^a	$H\alpha$ ^b	$\text{He I } \lambda 5876$ ^b	$H\beta$ ^b	$\text{He II } \lambda 4686$ ^b	$H\gamma$ ^b	$F_\lambda(5177 \text{ \AA})$ ^c
49517.845	1033.2 \pm 24.3	35.7 \pm 3.1	151.3 \pm 3.9	1.03 \pm 0.04
49595.389	1.28 \pm 0.05
49595.400	957.6 \pm 13.1	47.1 \pm 2.5
49595.411	155.5 \pm 4.4	39.9 \pm 4.3
49597.435	950.8 \pm 28.5

NOTE.—Table 9 appears in its entirety in the electronic edition of the *Astrophysical Journal Supplement Series*.

^a Julian Date – 2,400,000.

^b Units: $10^{-15} \text{ ergs s}^{-1} \text{ cm}^{-2}$.

^c Units: $10^{-15} \text{ ergs s}^{-1} \text{ cm}^{-2} \text{ \AA}^{-1}$.

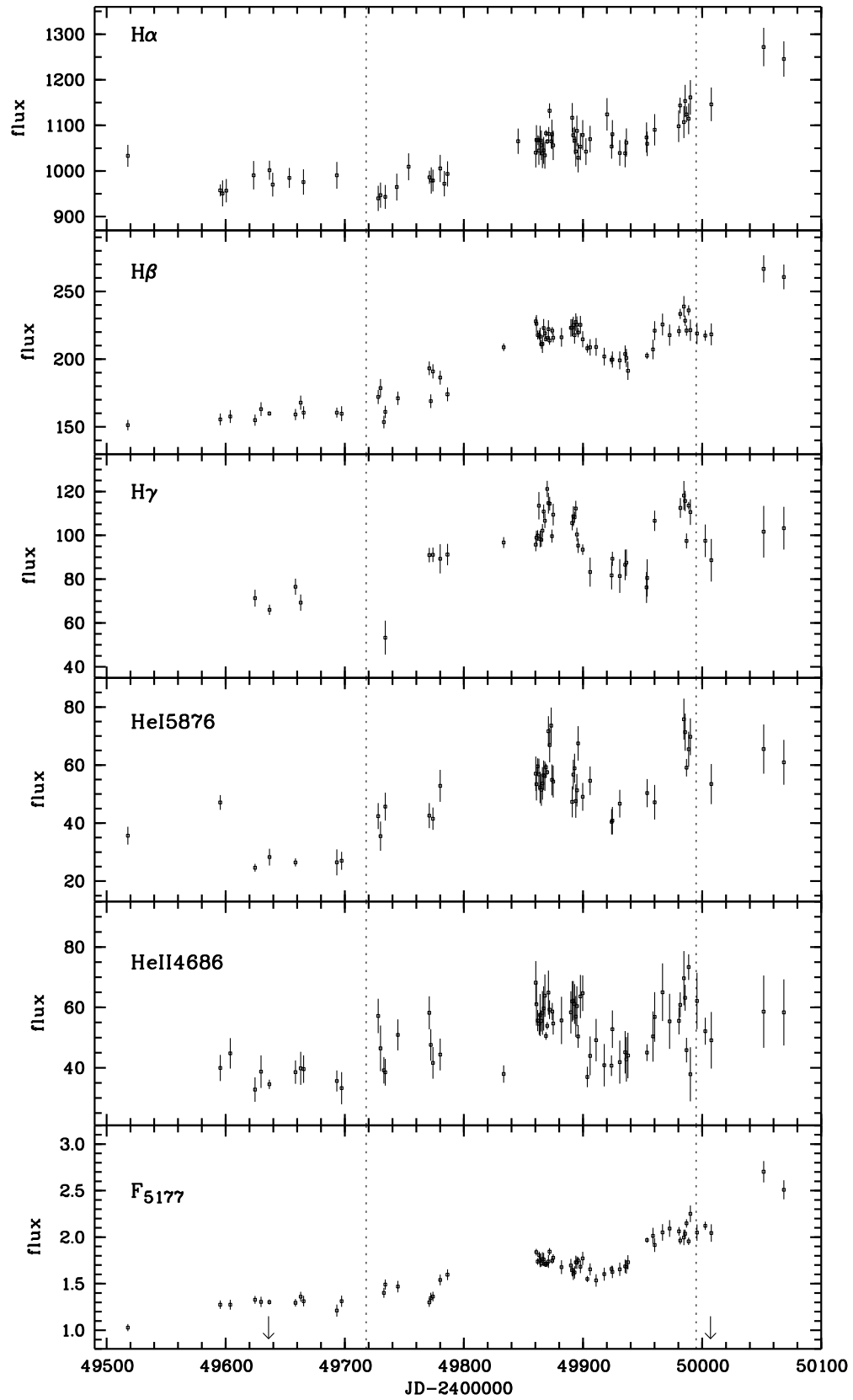


FIG. 4.—Light curves, as available on the WWW at the URL given above as Table 9, for the emission lines H α , H β , H γ , He I λ 5876, and He II λ 4686 and the optical continuum flux $F_{\lambda}(5177 \text{ \AA})$. The vertical scale is in units of $10^{-15} \text{ ergs s}^{-1} \text{ cm}^{-2}$ for the lines and $10^{-15} \text{ ergs s}^{-1} \text{ cm}^{-2} \text{ \AA}^{-1}$ for the continuum. The dashed vertical lines mark the temporal range of the X-ray observations.

TABLE 10
COMPARISON OF UNCERTAINTY
ESTIMATES

Feature	σ_{est}^a	σ_{obs}^b
<i>B</i>	0.036	0.027
<i>V</i>	0.048	0.043
<i>R</i>	0.020	0.015
<i>I</i>	0.019	0.018
H γ	0.062	0.055
He II $\lambda 4686$	0.145	0.137
H β	0.025	0.031
$F_\lambda(5177 \text{ \AA})$	0.040	0.041
He I $\lambda 5876$	0.106	0.099
H α	0.028	0.029

^a Mean fractional uncertainty based on point-to-point differences between closely spaced (i.e., $\Delta t \leq 2$ days) measurements.

^b Observational uncertainty based on uncertainties assigned to individual points.

lines. For the continuum, the mean fractional error (σ_{obs}) in a given measurement is 0.041. The average fractional uncertainty from the quoted estimate (σ_{est}) for the same measurements (Table 10) is 0.040, which implies that the error estimates are probably quite good. Generally, the estimated errors (σ_{est}) are of the same order as the observational uncertainties (σ_{obs}) derived directly from the measurements.

A comparison of the flux of the broadband measurements and the broad emission lines is given in Table 11. The mean spectroscopic continuum flux is lower than the mean broadband *V*- and *R*-flux. This can be explained by the fact that the broadband flux measurements contain in addition to the continuum flux emission-line contributions. The variability parameter F_{var} and R_{max} have been calculated for the broadband flux variations (see Clavel et al. 1991; Rodríguez-Pascual et al. 1997). The quantity R_{max} is simply the ratio of the maximum to the minimum flux. The quantity F_{var} is an estimation of the fluctuations of the intrinsic variations relative to the mean flux. Therefore, the rms of the light curves has been corrected with respect to the uncertainties introduced by the observations. R_{max} and F_{var} of the broadband variations are given in Table 11.

3.2. Mean and Root Mean Square Spectra

We calculated the mean and root mean square (rms) spectra from the flux-scaled spectra, and the H α and H β regions are shown in Figure 5. The velocity scale is set by adopting a redshift $z = 0.0556$ given by the narrow com-

TABLE 11
VARIABILITY STATISTICS OF THE ENTIRE LIGHT CURVES

Feature	Mean Flux ^a	rms Flux ^a	R_{max}	F_{var}
<i>B</i>	2.55	0.36	1.69	0.124
<i>V</i>	2.62	0.41	1.98	0.127
<i>R</i>	2.08	0.21	1.57	0.083
<i>I</i>	1.33	0.12	1.49	0.070
H γ	96.5	14.9	2.27	0.093
He II $\lambda 4686$	51.5	10.3	2.61	0.131
H β	206.4	24.6	1.76	0.088
$F_\lambda(5177 \text{ \AA})$	1.7	0.3	2.63	0.122
He I $\lambda 5876$	52.8	12.2	3.08	0.130
H α	1056.0	64.8	1.35	0.032

^a Continuum flux and broadband fluxes in units of $10^{-15} \text{ ergs s}^{-1} \text{ cm}^{-2} \text{ \AA}^{-1}$; line fluxes in units of $10^{-15} \text{ ergs s}^{-1} \text{ cm}^{-2}$.

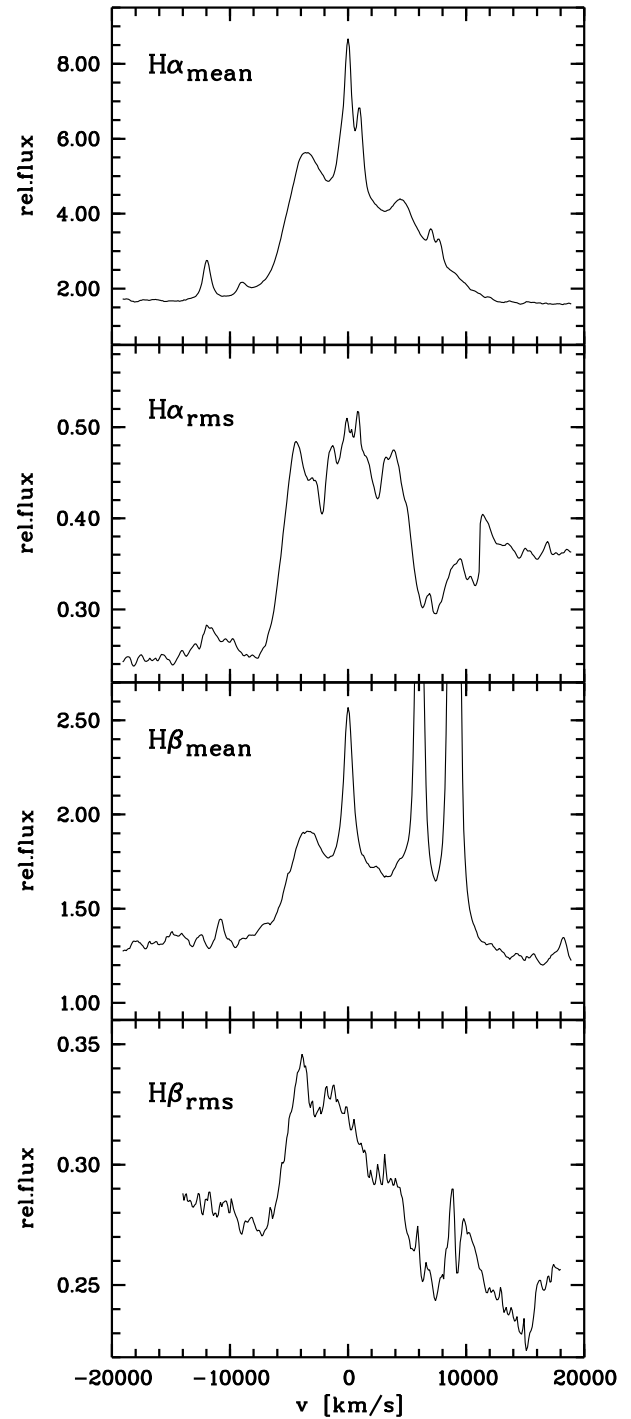


FIG. 5.—The mean and root mean square (rms) spectra in the vicinity of H α (top) and H β (bottom). The vertical scales are arbitrary. The rms spectra highlight the most variable parts of the emission-line profiles. In the H α rms spectrum, narrow residuals of [O I] $\lambda 6300$ are visible, and the narrow residual of [O III] $\lambda 5007$ can be seen in the H β rms spectrum; these are due to imperfect relative scaling of spectra from different sources.

ponents of H α and H β and the [O III] $\lambda\lambda 4959, 5007$ emission lines, i.e., the rest frame of the NLR. The rms spectrum is useful for isolating the variable parts of the line profile. The full width at zero intensity (FWZI) of the mean H α and H β profiles is $(25,000 \pm 2000) \text{ km s}^{-1}$, while the FWZI of the rms profiles is only $(14,000 \pm 500) \text{ km s}^{-1}$ (see Fig. 5). Thus, the variations in the broad emission line profiles are strong at lower radial velocities, while the flux originating in

high radial-velocity gas varies little, if at all. This behavior is similar to what has been seen in Mrk 590 (Ferland, Korista, & Peterson 1990; Peterson et al. 1993).

The line profiles of H α and H β show clear asymmetric structure. At least three substructures can be identified in both line profiles. A blue hump in the mean spectra is located near -3500 km s^{-1} with respect to the line peak, and a red hump is seen near $+4300 \text{ km s}^{-1}$. The red and blue humps can be seen clearly in the rms spectra, and in addition a broad central component appears. If these three components are modeled as Gaussians, the FWHM of the components in the wings is of order 3000 km s^{-1} , while for the central component the FWHM is $\sim 4000 \text{ km s}^{-1}$. The components in the profile wings are nearly symmetrically located with respect to the line center.

In the rms spectrum of the H β emission line, a strong broad feature at $\sim 10,000 \text{ km s}^{-1}$ is clearly visible. The FWHM of the structure can be estimated to $\sim 3500 \text{ km s}^{-1}$. The residuals of the narrow [O III] lines are located at $\sim 6000 \text{ km s}^{-1}$ and $\sim 8900 \text{ km s}^{-1}$. Since this feature is also visible in the rms spectrum of H α and of H γ , it cannot be caused entirely by inaccurate scaling of the NLR contribution of the narrow [O III] lines. Furthermore, in the difference spectrum of the low and high state of 3C 390.3 during this monitoring campaign (see Fig. 3), a strong broad feature is clearly visible at the red side of H α ($\sim 7150 \text{ \AA}$) and a weaker structure at the red side of H β ($\sim 5300 \text{ \AA}$). The analysis of the simultaneous ultraviolet campaign reveals the existence of a feature at $\sim 8500 \text{ km s}^{-1}$ in the outer red wing of the C IV $\lambda 1548$ emission line (O'Brien et al. 1998).

3.3. Time-Series Analysis

In order to quantify any possible time delay between the various light curves shown in Figures 1 and 4, we perform a simple cross-correlation analysis. Three methods that are commonly used in AGN variability studies have been used to compute cross-correlation functions (CCFs)—the interpolated cross-correlation function (ICCF) of Gaskell & Sparke (1986) and Gaskell & Peterson (1987), the discrete correlation function (DCF) of Edelson & Krolik (1988), and the z -transformed discrete correlation function method (ZDCF) of Alexander (1997). The ICCF and DCF algorithms and the limitations of the methods have been discussed in detail by Robinson & Pérez (1990) and by White & Peterson (1994), and the specific implementation of the ICCF and DCF used here are as described by White & Peterson (1994).

The emission lines are expected to change in response to variations in the far-UV continuum, primarily to the unobservable wavelengths just shortward of 912 \AA . We must therefore assume that the observable continuum can approximate the behavior of the ionizing continuum. It is generally assumed in this type of analysis that the shortest observed UV wavelength provides the best observable approximation to the “driving” (ionizing) continuum. For the first time, however, we have a well-sampled simultaneous soft X-ray light curve (Leighly et al. 1997), so we can compare the X-ray and UV continua (O'Brien et al. 1998) directly. In this analysis, we used the X-ray light curve as the driving continuum (Fig. 6) since the observational uncertainties are smaller than for the UV light curve. As will be discussed elsewhere (O'Brien et al. 1998), the relative amplitudes of the ultraviolet variations at a wavelength of 1370 \AA are nearly identical to those in the *ROSAT* HRI light curve, so the results presented here do not depend critically on our choice of the X-ray light curve in preference to the UV light curve.

Since the sampling of the B -band light curve is very poor, we have excluded the B -band data from the cross-correlation analysis. Operationally, the temporal coverage of the optical light curves was restricted to the period covered by the X-ray measurements. All of the light curves were binned into time intervals of 0.5 days to avoid unnecessary structure in the ICCF. For each light curve, we also computed the sampling-window autocorrelation function (ACF_{sw}), which is a measure of how much of the width of the ACF is introduced by the interpolation process rather than by real correlation of the continuum values at different times. The ACF_{sw} is computed by repeatedly sampling white noise light curves in exactly the same way as the real observations and then computing the autocorrelation function (ACF). The average of many such autocorrelations, the ACF_{sw} , has a peak at zero lag whose width depends on how much interpolation the ICCF has to do on short timescales. The width (FWHM) of the ACF_{sw} is 1.8 ± 0.3 days for the emission lines and broadband flux measurements for the X-ray restricted time period. These values are negligible compared to the widths of any of the emission-line ACFs or CCFs found here (see Figs. 7–9), and thus interpolation of the light curves is justified.

The general sampling characteristics of each of the restricted and rebinned light curves are given in Table 12. The name of the feature is given in column (1), and column (2) gives the total number of points N in the light curve that

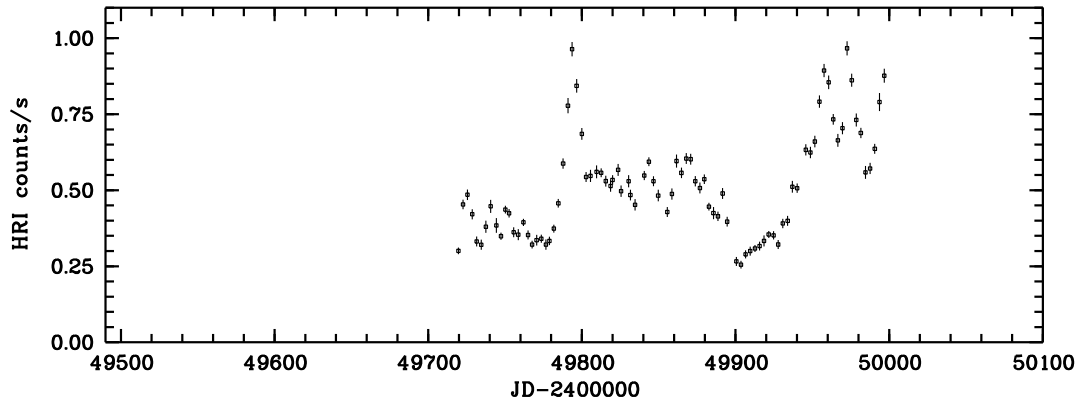


FIG. 6.—*ROSAT* HRI light curve from monitoring observation of 3C 390.3 (see Leighly et al. 1997)

TABLE 12
SAMPLING CHARACTERISTICS^a

FEATURE (1)	N (2)	FWHM		ACF _{sw} (days) (5)
		ACF (3)	ICCF (4)	
V	126	89	53	1.5
R	104	121	50	2.0
I	82	132	53	2.5
$F_{\lambda}(5177 \text{ \AA})$	55	69	53	1.8
H γ	42	36	49	1.7
He II $\lambda 4686$	58	8	33	1.8
H β	59	64	52	1.8
He I $\lambda 5876$	40	6	55	1.5
H α	54	105	56	1.7

^a X-ray-restricted and rebinned light curves.

are used in computing the cross-correlation functions. The width (FWHM) of the ACF is given in column (3), and the width of ICCF computed by cross-correlation with the X-ray continuum is given in column (4). Column (5) gives the width (FWHM) of the corresponding ACF_{sw}.

Uncertainties in the ICCF results for the cross-correlation maxima and centroids, $\Delta\tau_{\max}$ and $\Delta\tau_{\text{cent}}$, respectively, were computed through Monte Carlo techniques as

follows: for both time series, each flux value in the light curves was modified with Gaussian deviates based on the quoted uncertainty for that point. Each light curve of N points was then randomly resampled N times in a “bootstrap” fashion, specifically allowing points to appear more than one time (the effect of which is only to remove at random certain points from the light curve). The ICCF was computed, and the values of τ_{\max} and τ_{cent} were recorded if they were statistically significant at a confidence level higher than 95% and not clear outliers (e.g., lags larger than 100 days). By repeating this process 500–1000 times, distributions of τ_{\max} and τ_{cent} were built up. The means of these distributions were always very close to the values of τ_{\max} and τ_{cent} obtained from the original series, and the standard deviations of these distributions are taken to be the uncertainty associated with a single realization, i.e., the quoted uncertainties $\Delta\tau_{\max}$ and $\Delta\tau_{\text{cent}}$.

The ACF, ACF_{sw}, ICCF, and ZDCF are shown for the broadband variations in V , R , and I (Fig. 7), the broad Balmer emission lines H α , H β , and H γ (Fig. 8), the helium lines He I $\lambda 5876$ and He II $\lambda 4686$, and the optical continuum $F_{\lambda}(5177 \text{ \AA})$ (Fig. 9). The ACFs of the light curves are broad since the shape is dominated by the nearly monotonic increase in the light curves. The FWHMs of the ACFs of the well-sampled light curves are of the order of 50–100 days

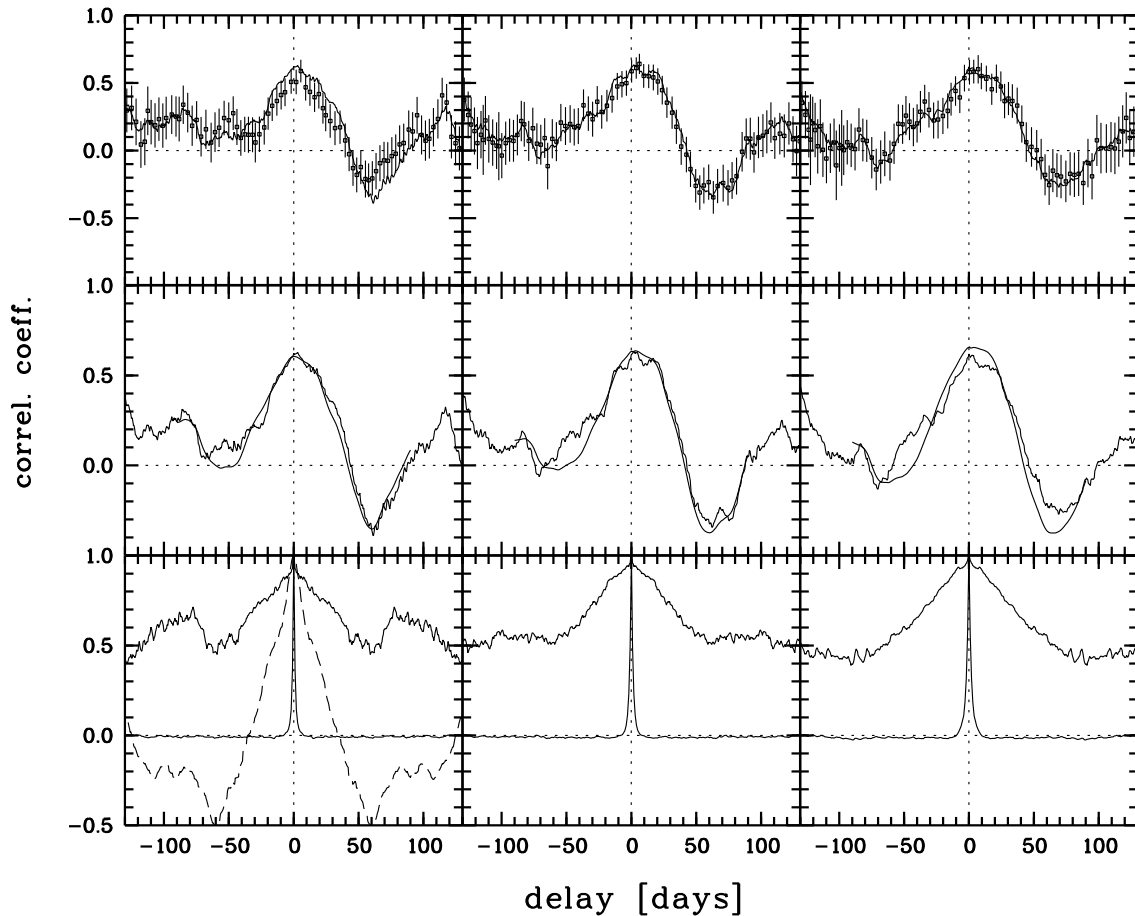


FIG. 7.—The bottom row of panels shows the broad autocorrelation functions (ACFs) and corresponding narrow sampling window autocorrelation functions (ACF_{sw}) for the broadband V , R , and I fluxes (left to right) available as Table 2 on the WWW at the URL given above. In the lower left-hand panel, the ACF of the X-ray variations is shown as a long-dashed line for comparison with the ACFs of the optical variations. In the middle row of panels, the ICCF is displayed together with the corresponding mean ICCF, which is calculated within the routine to compute the cross-correlation peak distribution (CCPD) (see Maoz & Netzer 1989). The smooth curve of the simulated mean ICCF and the ICCF of the real observations are very similar. The top row of panels shows the results of cross-correlating each of these light curves with the simultaneous X-ray light curve from Leighly et al. (1997). The ICCF is shown as a connected line, and the ZDCF is shown as individual points with associated error bars.

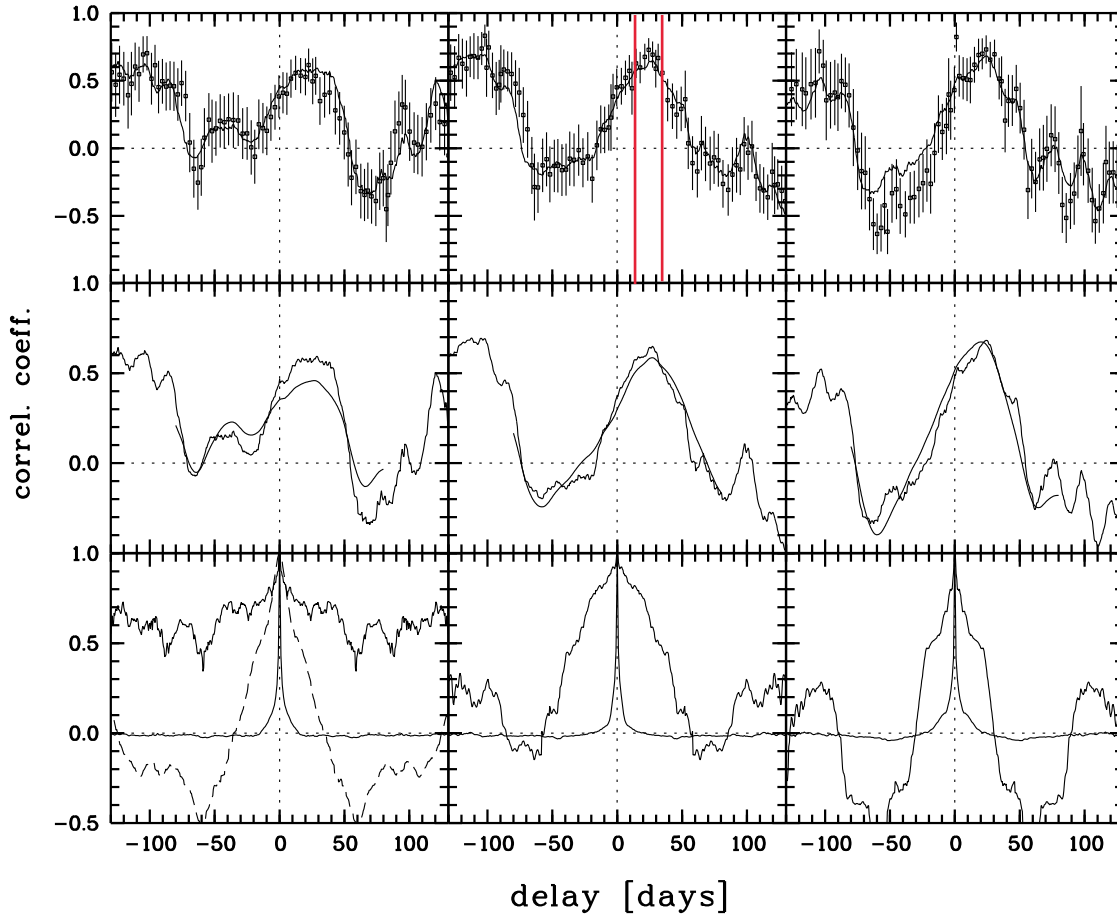


FIG. 8.—Cross-correlation functions for the broad Balmer emission lines H α , H β , and H γ (left to right). The cross-correlation functions are plotted as in Fig. 7.

(Table 12). Within the uncertainties, the DCFs and ZDCFs are identical; therefore, to avoid confusion, only the ICCFs and the corresponding ZDCF are displayed in Figures 7–9.

The time delay derived from the centroid of a cross-correlation function provides a more robust estimate of the lag than does the peak, as evidenced by the consistently smaller widths of the Monte Carlo distributions for the centroid compared to the peak. Also, in the case of the emission lines, the centroid is readily identified with a physically meaningful quantity, the luminosity-weighted radius

of the line-emitting region (Koratkar & Gaskell 1991). The delays expressed by τ_{cent} of the three methods used here are nearly identical within the uncertainties, although the DCF method tends to yield smaller delays than the ICCF and ZDCF method.

The results of the cross-correlation analysis are given in Table 13. Column (1) indicates the “responding” light curve (i.e., the light curve that is assumed to be responding to the driving light curve), and column (2) gives the peak value of the correlation coefficient r_{max} for the ICCF. The position of

TABLE 13
CROSS-CORRELATION RESULTS^a

FEATURE (1)	r_{max} (2)	τ_{max} (days)			$\Delta\tau_{\text{max}}$ (days) (6)	τ_{cent} (days)			$\Delta\tau_{\text{cent}}$ (days) (10)
		ICCF (3)	ZDCF (4)	DCF (5)		ICCF (7)	ZDCF (8)	DCF (9)	
V	0.62	3.5	5.3	4.9	4.5	3.5	5.0	5.0	3.0
R	0.63	3.5	4.8	3.8	5.6	5.5	5.8	4.0	3.9
I	0.61	3.5	4.5	3.7	6.2	7.9	7.0	4.7	4.2
$F_{\lambda}(5177 \text{ \AA})^b$	0.73	−2.5	8.3	11.4	6.2	5.3	8.5	8.5	2.8
H γ	0.66	24.5	23.7	24.1	6.2	16.8	13.8	20.8	5.5
He II $\lambda 4686$	0.37	13.0	5.9	10.4	8.3	8.6	4.6	17.8	7.8
H β	0.64	24.5	24.4	12.5	5.3	22.9	23.2	15.4	3.9
He I $\lambda 5876$	0.69	25.0	23.4	11.4	9.5	18.6	22.6	17.2	8.5
H α	0.53	29.0	18.7	11.2	10.3	19.3	20.6	15.9	9.5

^a Light curves restricted approximately to the period of X-ray monitoring, JD 2,449,719–JD 2,449,997.

^b Light curves restricted approximately to the period of overlap, JD 2,449,732–JD 2,449,996.

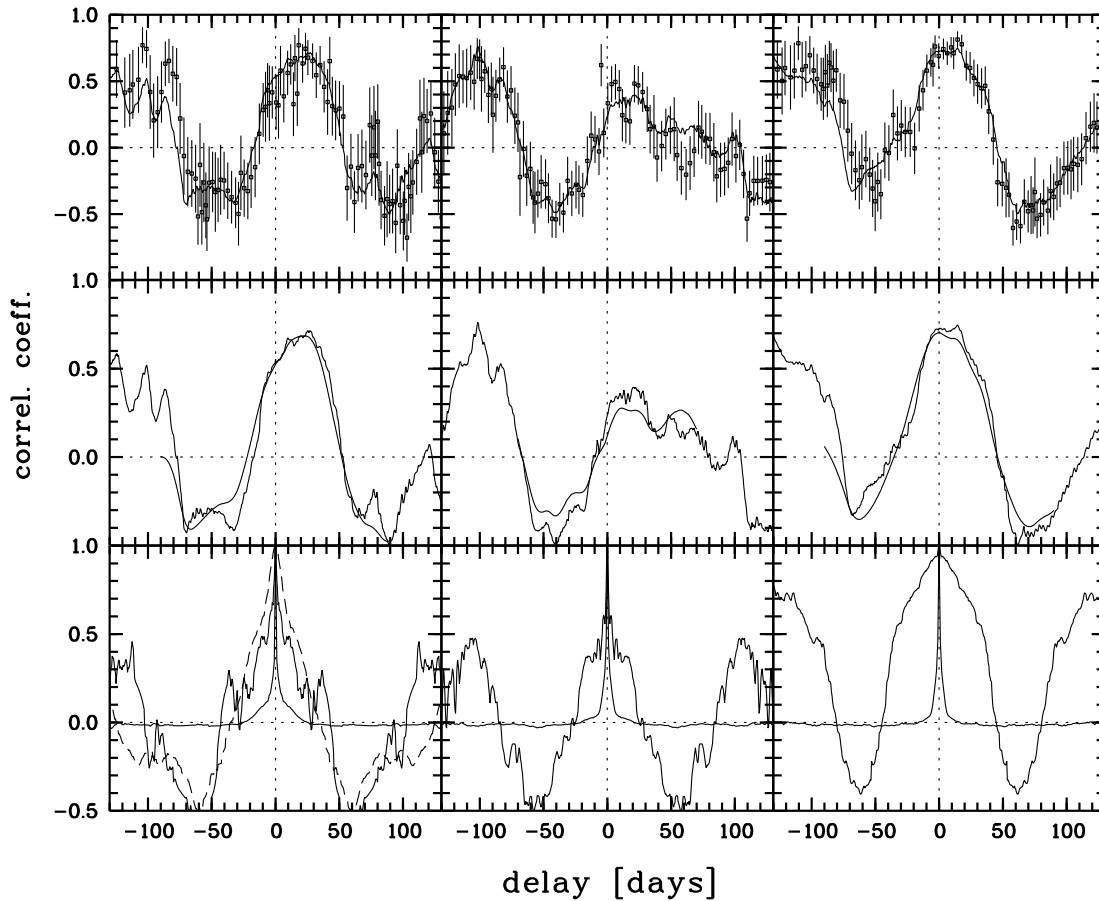


FIG. 9.—Cross-correlation functions for the He I $\lambda 5876$ and He II $\lambda 4686$ emission lines, and for the spectrophotometric optical continuum flux $F_{\lambda}(5177 \text{ \AA})$ (left to right). The cross-correlation functions are plotted as in Fig. 7.

the peak of the cross-correlation functions τ_{\max} was measured by fitting a Gaussian curve to the upper 85% of the ICCF, ZDCF, and DCF; these values are given in columns (3), (4), and (5), respectively, and column (6) gives the error estimate for the position of the cross-correlation peak $\Delta\tau_{\max}$. The centroids τ_{cent} of the ICCF, ZDCF, and DCF, in each case computed using the points in the cross-correlation function with values greater than $0.8r_{\max}$, are given in columns (7), (8), and (9), respectively, and the uncertainty in the ICCF centroid $\Delta\tau_{\text{cent}}$ is given in column (10).

The broadband (V , R , and I) and the optical continuum flux variations appear to be delayed by a few days, relative to the X-ray or ultraviolet continuum variations. However, the measured lags are in no case different from zero at any reasonable level of statistical significance if the Monte Carlo-based error estimates are reliable. Somewhat smaller, but marginally statistically significant, wavelength-dependent continuum lags have been reported in the case of NGC 7469 (Wanders et al. 1997; Collier et al. 1998), although in the case of NGC 7469 the mean spacing between observations of the driving continuum is much smaller than for the observations reported here.

The emission-line time delays are similar for all of the optical emission lines, about 20 days, although in each case the uncertainties are somewhat larger than we have obtained in similar experiments because of the vagaries of the continuum behavior and sampling. Within the uncertainties, the measured time delays for $H\alpha$, $H\beta$, $H\gamma$, and He I

$\lambda 5876$ are indistinguishable. However, the uncertainties are sufficiently large that ionization stratification, as detected in other well-studied sources, also cannot be ruled out. Only He II $\lambda 4686$ appears to respond more rapidly than the other lines, but the relatively low value of r_{\max} and relatively narrow width of the cross-correlation function (about 30 days as compared to ~ 50 days for the other lines) cast some doubt on the significance of this result. In contrast to the AGNs studied before, the delay of the Ly α and C IV line variations of the current 3C 390.3 campaign is significantly larger than the delay of the optical lines. The analysis of the ultraviolet spectra yields a delay of 35–70 days for Ly α and C IV (O'Brien et al. 1998).

In order to study the response of individual parts of the line profile to the X-ray continuum variations and thus search for evidence of an organized radial-velocity field in the BLR, we have divided the profiles of the strongest and least contaminated lines, $H\alpha$ and $H\beta$, into three parts: the blue wing (-7500 to -2000 km s^{-1}), the core (-2000 to $+2000 \text{ km s}^{-1}$), and the red wing ($+2000$ to $+7500 \text{ km s}^{-1}$). The light curves of the different profile sections (see Figs. 10 and 11) were rebinned onto 0.5 day intervals (available in electronic form on the WWW at the URL given above as Table 14), and again cross-correlations were performed restricting the data to the X-ray monitoring period. Since we are concerned at this point with *differential* lags between different sections of the line profiles, we cross-correlate the light curves for the different line sections

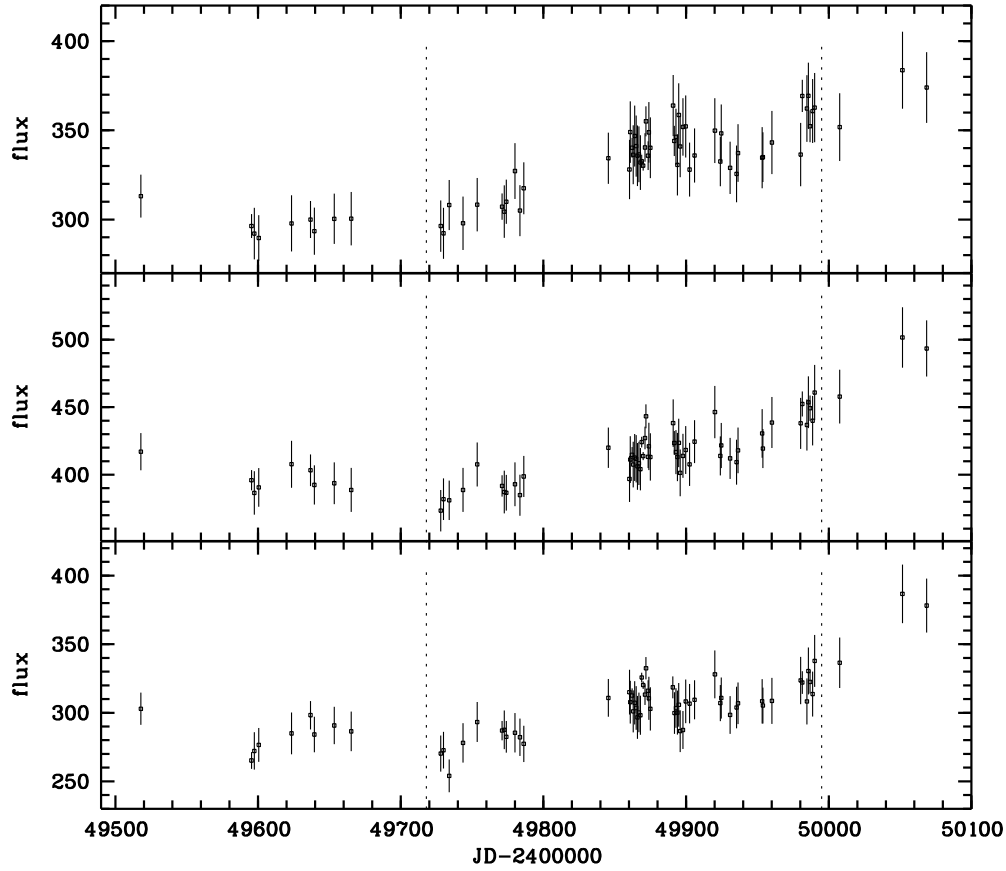


FIG. 10.—Light curves for each of the parts of the $H\alpha$ emission-line profile. The light curve of the blue wing is shown in the top panel, the middle panel displays the light curve of the line core, and at the bottom the light curve of the red wing is presented. The vertical scale is in units of 10^{-15} ergs s^{-1} cm^{-2} . The dashed vertical lines mark the temporal range of the X-ray observations.

against each other rather than against the driving continuum; we arbitrarily chose the line cores as the first (driving) series and computed the lags of the red and blue wings of the lines relative to the core. These results are shown in

Table 15 and in Figures 12 and 13. Neither $H\alpha$ nor $H\beta$ shows any evidence for any differences in the response of the wings relative to the core. In the case of $H\alpha$, the uncertainties are especially large because of the low amplitude of

TABLE 14
LIGHT CURVES

JD ^a	$H\alpha_{\text{blue}}^b$	$H\alpha_{\text{core}}^b$	$H\alpha_{\text{red}}^b$	$H\beta_{\text{blue}}^b$	$H\beta_{\text{core}}^b$	$H\beta_{\text{red}}^b$
49517.845	313.1 ± 12.0	417.1 ± 13.8	302.9 ± 11.8	39.0 ± 1.7	58.5 ± 1.7	53.7 ± 2.7
49595.400	296.4 ± 6.7	395.9 ± 7.5	265.2 ± 6.1
49595.411	44.6 ± 2.1	59.9 ± 1.9	51.0 ± 2.4
49597.435	292.1 ± 14.4	386.5 ± 16.1	272.2 ± 13.6
49600.436	289.6 ± 12.8	390.6 ± 14.4	276.5 ± 12.4

NOTE.—Table 14 appears in its entirety in the electronic edition of the *Astrophysical Journal Supplement Series*.

^a Julian Date $-2,400,000$.

^b Units: 10^{-15} ergs s^{-1} cm^{-2} .

TABLE 15
CROSS-CORRELATION RESULTS FOR LINE PROFILE SECTIONS^a

FIRST SERIES	SECOND SERIES	r_{max}	τ_{max} (days)			$\Delta\tau_{\text{max}}$ (days)	τ_{cent} (days)			$\Delta\tau_{\text{cent}}$ (days)
			ICCF	ZDCF	DCF		ICCF	ZDCF	DCF	
$H\beta_{\text{core}}$	$H\beta_{\text{bluewing}}$	0.89	0.0	1.0	−4.0	5.7	5.6	3.1	0.0	5.6
$H\beta_{\text{core}}$	$H\beta_{\text{redwing}}$	0.84	0.5	−1.2	0.0	8.6	0.3	0.4	8.8	8.7
$H\alpha_{\text{core}}$	$H\alpha_{\text{bluewing}}$	0.86	0.0	4.4	−4.0	18.4	3.9	2.1	−4.0	17.8
$H\alpha_{\text{core}}$	$H\alpha_{\text{redwing}}$	0.87	0.0	1.2	0.0	22.6	−0.5	−0.9	−1.9	19.0

^a Light curves restricted approximately to the period of X-ray monitoring, JD 2,449,719–JD 2,449,997.

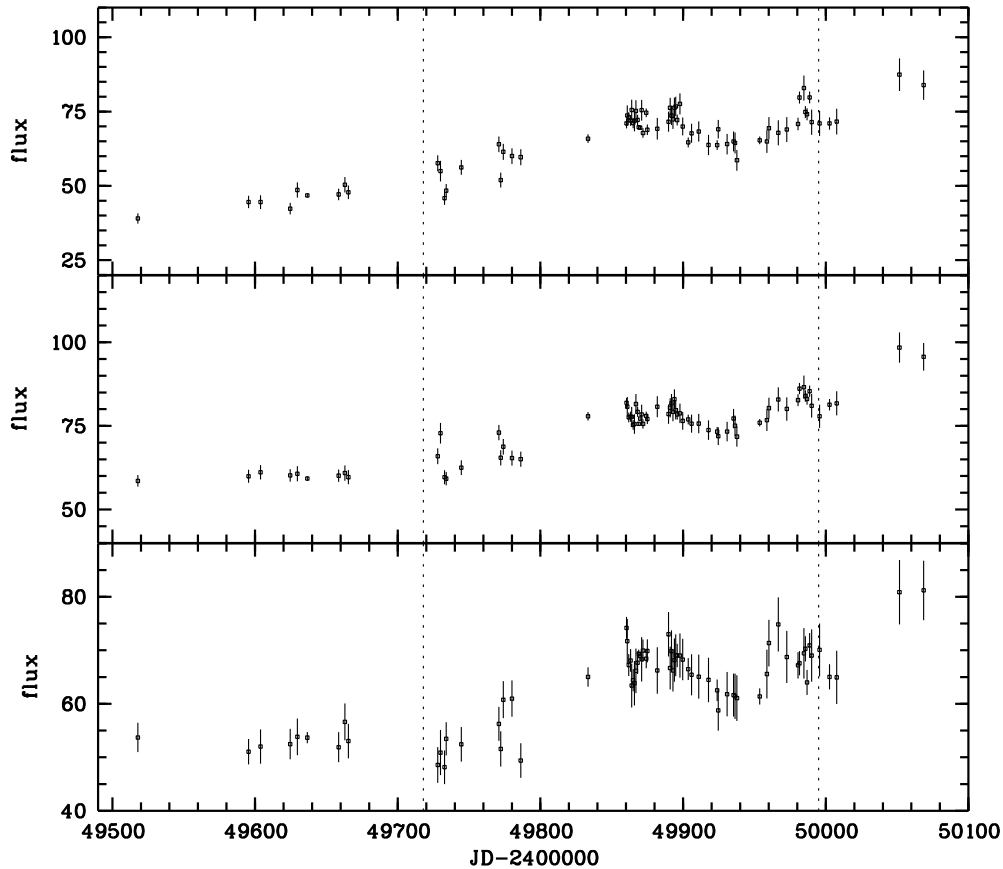


FIG. 11.—Light curves for each of the parts of the $H\beta$ emission-line profile. The light curve of the blue wing is shown in the top panel, the middle panel displays the light curve of the line core, and at the bottom the light curve of the red wing is presented. The vertical scale is in units of $10^{-15} \text{ ergs s}^{-1} \text{ cm}^{-2}$. The dashed vertical lines mark the temporal range of the X-ray observations.

variability, but the $H\beta$ results seem to exclude the possibility that the BLR velocity field is characterized by primarily radial motions, either infall or outflow.

4. SUMMARY

The results of a year-long (1994 October to 1995 October) optical monitoring campaign on the BLRG 3C 390.3 are presented in this paper. The principal findings are as follows:

1. The broadband (B , V , R , and I) fluxes, the optical continuum measured from spectrophotometry $F_\lambda(5177 \text{ \AA})$, and the integrated emission-line fluxes of $H\alpha$, $H\beta$, $H\gamma$, $\text{He I } \lambda 5876$, and $\text{He II } \lambda 4686$ showed significant variations of order 50% in amplitude.

2. The parameter F_{var} , which is essentially the rms variation about the mean, increased with decreasing wavelength for the broadband measurements as well as for the Balmer emission lines.

3. The variations of the broadband and emission-line fluxes are delayed with respect to the X-ray variations. Cross-correlation functions were calculated with three different methods (ICCF, DCF, and ZDCF). The time delays of the optical continuum variations expressed by the centroid of the cross-correlation functions are typically about 5 days, but with uncertainties of ~ 5 days. Therefore, zero-time delay between the high-energy and low-energy continuum variability cannot be ruled out. The delays of the Balmer lines $H\alpha$, $H\beta$, and $H\gamma$ and of $\text{He I } \lambda 5876$ are typically

around 20 ± 8 days. There is some evidence that $\text{He II } \lambda 4686$ responds somewhat more rapidly with a time delay of ~ 10 days, but again the uncertainties are quite large (~ 8 days).

4. The simple cross-correlation analysis of the line core with the line profile wings of the $H\alpha$ and $H\beta$ emission might indicate that the wings vary in the same way with respect to the line core. But there might be a weak indication that the variations of the blue wing are delayed by ~ 4 days with respect to the red wing.

5. The mean and rms $H\alpha$ and $H\beta$ line profiles reveal the existence of at least three substructures—a central component, plus strong blue and red components at about $\pm 4000 \text{ km s}^{-1}$ relative to line center. The rms spectra show that the broad-line variations are much stronger at line center than in the outer wings.

This work has been supported by SFB328D (Landessternwarte Heidelberg), by the NSF through grant AST 94-20080 (Ohio State University), AST 93-20715 (University of Arizona), AST 94-17213 (University of California, Berkeley), DFG grant KO 857/18-1 (Universitätssternwarte Göttingen), GSU Research Program Enhancement NASA grant NAGW-4397, Royal Society (University of Hertfordshire), Chinese NSF and Open Laboratory for Optical Astronomy of Chinese Academy of Sciences (Beijing Astronomical Observatory), PPARC research studentship and PPARC grant GRK/46026 (St. Andrews), Russian Basic Research Foundation

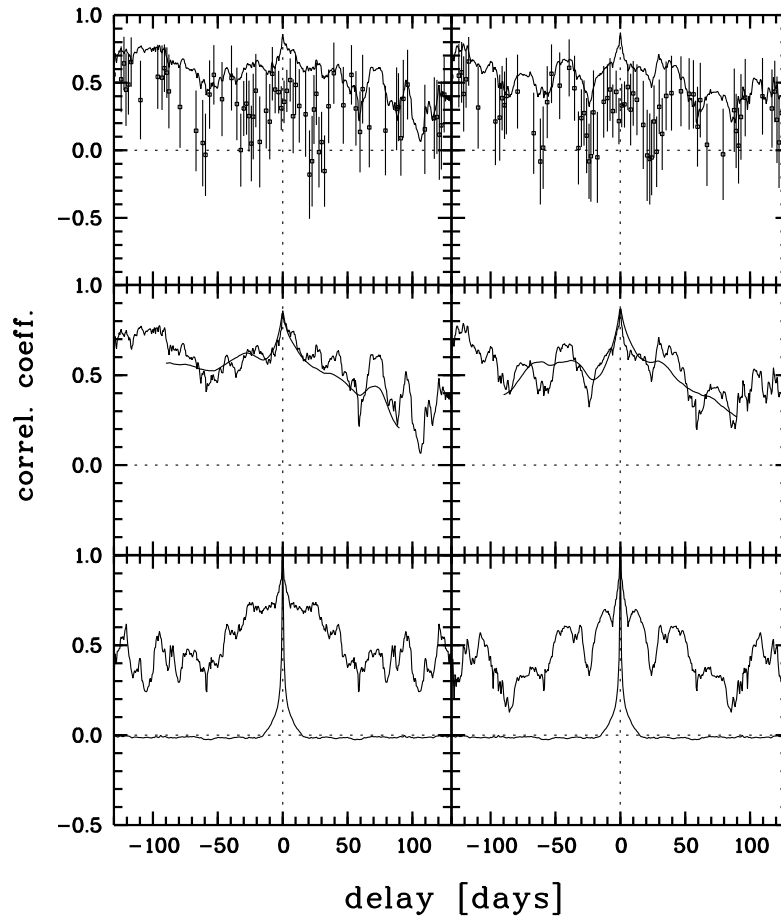


FIG. 12.—The top row of panels shows the results of cross-correlating the blue wing (*left-hand column*) and red wing (*right-hand column*) of the H α emission line with the line core. The ICCF is shown as a connected line, and the ZDCF is shown as individual points with associated error bars. In the middle row of panels, the ICCFs of the profile sections are displayed together with the corresponding mean ICCF, which is yielded by calculating the CCPD (see Maoz & Netzer 1989). The corresponding autocorrelation functions are displayed in the bottom row of panels.

grant N94-02-4885a, N97-02-17625 (Sternberg Astronomical Institute, Special Astrophysical Observatory), ESO C&EE grant A-01-057, National Science Foundation Research Experience for Undergraduates (REU): grant

AST 94-23922, and by the Valdosta State University Center for Faculty Development and Instructional Improvement grant. We thank the FLWO observers P. Berlind and J. Peters (J. Huchra).

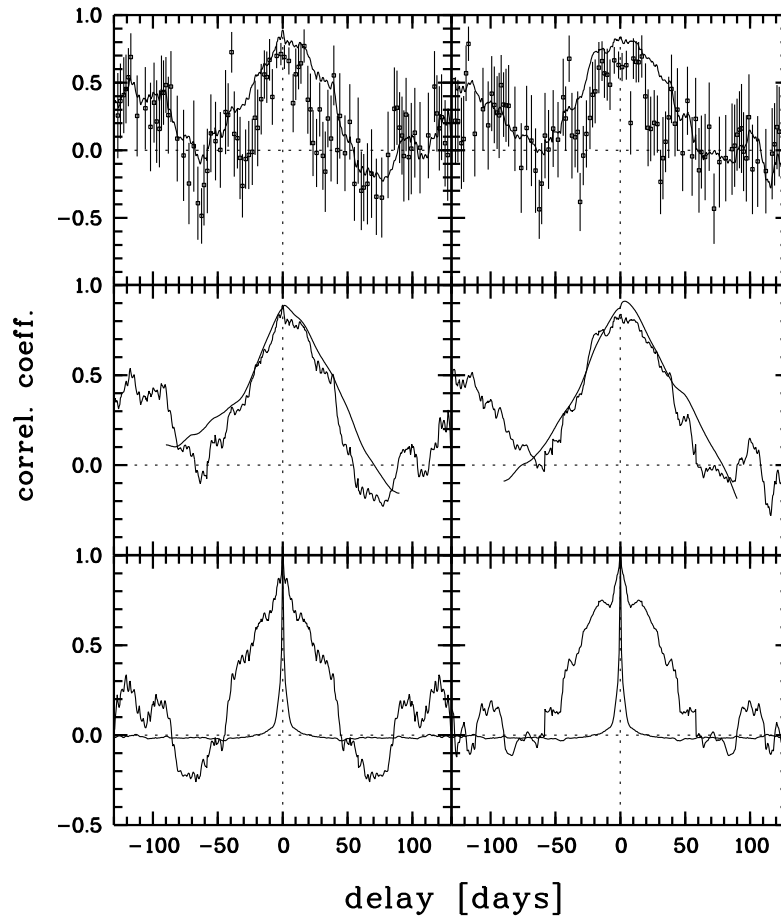


FIG. 13.—Cross-correlation functions of the broad $H\beta$ emission line sections. The results are plotted as in Fig. 12.

REFERENCES

- Alef, W., Wu, S. Y., Preuss, E., Kellermann, K. I., & Qui, Y. H. 1996, *A&A*, 308, 376
- Alexander, T. 1997, in *Astronomical Time Series*, ed. D. Maoz, A. Sternberg, & E. Leibowitz (Dordrecht: Kluwer), in press
- Allen, C. W. 1973, *Astrophysical Quantities* (London: Athlone)
- Alloin, D., Clavel, J., Peterson, B. M., Reichert, G. A., & Stirpe, G. M. 1994, in *Frontiers of Space and Ground-based Astronomy*, ed. W. Wamsteker, M. S. Longair, & Y. Kondo (Dordrecht: Kluwer), 423
- Alloin, D., et al. 1995, *A&A*, 293, 293
- Barr, P., et al. 1980, *MNRAS*, 193, 549
- Baum, S. A., Heckman, T., Bridle, A., van Breugel, W., & Miley, G. 1988, *ApJS*, 68, 643
- Christian, C. A., et al. 1985, *PASP*, 97, 363
- Clavel, J., et al. 1991, *ApJ*, 366, 64
- Clavel, J., & Wamsteker, W. 1987, *ApJ*, 320, L9
- Collier, S., et al. 1998, in preparation
- Crenshaw, D. M., et al. 1996, *ApJ*, 470, 322
- Dietrich, M., et al. 1993, *ApJ*, 408, 416
- Edelson, R. A., & Krolik, J. H. 1988, *ApJ*, 333, 646
- Edelson, R. A., et al. 1996, *ApJ*, 470, 364
- Ferland, G. J., Korista, K. T., & Peterson, B. M. 1990, *ApJ*, 363, L21
- Gaskell, C. M., & Peterson, B. M. 1987, *ApJS*, 65, 1
- Gaskell, C. M., & Sparke, L. S. 1986, *ApJ*, 333, 646
- Kaspi, S., et al. 1996, *ApJ*, 470, 336
- Koratkar, A. P., & Gaskell, C. M. 1991, *ApJS*, 75, 719
- Korista, K. T., et al. 1995, *ApJS*, 75, 719
- Leahy, J. P., & Perley, R. A. 1995, *MNRAS*, 277, 1097
- Leighly, K. M., et al. 1997, *ApJ*, 483, 767
- Lynds, C. R. 1968, *AJ*, 73, 888
- Maoz, D., & Netzer, H. 1989, *MNRAS*, 236, 21
- Maoz, D., et al. 1993, *ApJ*, 404, 576
- O'Brien, P. T., et al. 1998, *ApJS*, submitted
- Osterbrock, D. E., Koski, A. T., & Phillips, M. M. 1975, *ApJ*, 197, L41
- Penston, M. J., Penston, M. V., & Sandage, A. 1971, *PASP*, 83, 783
- Penston, M. V., & Pérez, E. 1984, *MNRAS*, 211, 33
- Peterson, B. M. 1993, *PASP*, 105, 247
- Peterson, B. M., & Collins, G. W., II. 1983, *ApJ*, 270, 71
- Peterson, B. M., et al. 1991, *ApJ*, 368, 119
- . 1993, *ApJ*, 402, 469
- . 1994, *ApJ*, 425, 622
- Peterson, B. M., Pogge, R. W., Wanders, I., Smith, S. M., & Romanishin, W. 1995, *PASP*, 107, 579
- Reichert, G. A., et al. 1994, *ApJ*, 425, 582
- Robinson, A., & Pérez, E. 1990, *MNRAS*, 244, 138
- Rodríguez-Pascual, P. M., et al. 1997, *ApJS*, 110, 9
- Sandage, A. R. 1966, *ApJ*, 145, 1
- Santos-Lleó, M., et al. 1997, *ApJS*, 112, 271
- Schild, R. E. 1983, *PASP*, 95, 1021
- Selmes, R. A., Tritton, K. P., & Wordsworth, R. W. 1975, *MNRAS*, 170, 15
- Smith, E. P., & Heckman, T. M. 1989, *ApJ*, 341, 658
- Stirpe, G. M., et al. 1994, *ApJ*, 425, 609
- van Groningen, E., & Wanders, I. 1992, *PASP*, 104, 700
- Veilleux, S., & Zheng, W. 1991, *ApJ*, 377, 89
- Wanders, I., et al. 1997, *ApJS*, 113, 69
- Wamsteker, W. 1981, *A&A*, 97, 329
- Wamsteker, W., Ting-gui, W., Scharrel, N., & Vio, R. 1997, *MNRAS*, 288, 225
- Warwick, R., et al. 1996, *ApJ*, 470, 349
- Wills, B. J., Netzer, H., & Wills, D. 1985, *ApJ*, 288, 94
- White, R. J., & Peterson, B. M. 1994, *PASP*, 106, 879
- Zheng, W. 1996, *AJ*, 111, 1498
- Zheng, W., Pérez, E., Grandi, S. A., & Penston, M. V. 1995, *AJ*, 109, 2355